Appl. Magn. Reson. 30, 251–268 (2006)

Applied Magnetic Resonance

Theoretical Investigation of $Q_A^{-\bullet}$–Ligand Interactions in Bacterial Reaction Centers of *Rhodobacter sphaeroides*

J. Fritscher, T. F. Prisner, and **F. MacMillan**

Institut für Physikalische und Theoretische Chemie and Center for Biomolecular Magnetic Resonance, J. W. Goethe-Universität, Frankfurt am Main, Germany

Received May 23, 2006; revised July 6, 2006

Abstract. Density functional theory was used to calculate magnetic resonance parameters for the primary stable electron acceptor anion radical ($Q_A^{-\bullet}$) in its binding site in the bacterial reaction center (bRC) of *Rhodobacter sphaeroides*. The models used for the calculations of the $Q_A^{-\bullet}$ binding pocket included all short-range interactions of the ubiquinone with the protein surroundings in a gradual manner and thus allowed a decomposition and detailed analysis of the different specific interactions. Comparison of the obtained hyperfine and quadrupole couplings with experimental data demonstrates the feasibility and reliability of calculations on such complex biologically relevant systems. With these results, the interpretation of previously published 3-pulse electron spin echo envelope modulation data could be extended and an assignment of the observed double quantum peak to a specific amino acid is proposed. The computations provide evidence for a slightly altered binding site geometry for the Q_A ground state as investigated by X-ray crystallography with respect to the $Q_A^{-\bullet}$ anion radical state as accessible via EPR spectroscopy. This new geometry leads to improved fits of the W-band correlated-coupled radical pair spectra of $Q_A^{-\bullet}$-$P_{865}^{+\bullet}$ compared to orientation data from the crystal structure. Finally, a correlation of the ^{14}N quadrupole parameters of His219 with the hydrogen bond geometry and a comparison with previous systematic studies on the influence of hydrogen bond geometry on quadrupole coupling parameters (J. Fritscher: Phys. Chem. Chem. Phys. 6, 4950–4956, 2004) is presented.

1 Introduction

Magnetic resonance spectroscopic techniques [1, 2] such as electron paramagnetic resonance (EPR), electron–nuclear double resonance (ENDOR) or electron spin echo envelope modulation (ESEEM) can provide quadrupole coupling (QC) and hyperfine coupling (HFC) tensor eigenvalues and orientations. Due to various reasons, however, e.g., lack of single crystals, overlap of spectral lines or line broadening effects, it is often not possible to extract all the spectral information, to assign all coupling constants to the different interacting nuclei or to relate relative tensor orientations to the molecular or *g*-tensor frame. It has been shown that density functional theory [3] (DFT) calculations are capable of predicting

such HFC tensors for organic radicals [4–7], whereas the treatment of transition metal systems is also possible but in general much more difficult [7–10]. There are also systematic DFT studies of QC tensors for different nuclei and molecules that demonstrate the reliability of such theoretical predictions [11–19]. These results suggest that quantum chemical calculations based on the (unrestricted) Kohn–Sham formalism can be the missing link between magnetic resonance data and molecular structure. It is now desirable to extend the systems under consideration to (macro)molecules involved in important biological processes. This approach has so far been successfully applied to study, e.g., [NiFe] hydrogenase [20, 21], B_{12}-dependent glutamate mutase [22], (bacterio-)chlorophylls [23, 24], blue copper proteins [25, 26], coenzyme B_{12} [27], small α-helix and β-sheet protein fragments [28], the hammerhead ribozyme [29], ribonucleotide reductase [30], cytochrome P450 [31] and quinol oxidase [32].

The first stable electron acceptor, Q_A (a ubiquinone-10 molecule), from bacterial reaction centers (bRCs) of *Rhodobacter sphaeroides* plays an important role in the electron transfer processes of bacterial photosynthesis [33, 34]. It serves as a one-electron acceptor and donor in the light-induced electron transport chain. Q_A receives an electron from a bacteriopheophytin anion radical, is reduced to $Q_A^{-\bullet}$ and passes the electron on to the isostructural secondary quinone acceptor Q_B within about 200 μs. In contrast to Q_B, which successively accepts two electrons and two protons and then leaves its binding site as Q_BH_2, Q_A only alternates between the fully oxidized and anionic semiquinone state and never becomes fully reduced. The two ubiquinones Q_A and Q_B act as a two-electron gate transducing the one-electron photochemical excitation event into a two-electron transfer process. The different redox or magnetic properties of the two isostructural ubiquinones must result from different binding environments in the protein [35]. Q_A is positioned in a well defined rigid binding pocket constituted by the amino acid residues His219, Trp252, Ala260 and Ile265 (see Fig. 1). From the crystal structure [36] it is suggested to be bound to the protein surroundings via two hydrogen bonds to the NH group of the His219 imidazole ring and the backbone NH group of Ala260. Q_A has been thoroughly studied previously by EPR, ENDOR and ESEEM spectroscopy (for a review see ref. 35 and references therein as well as ref. 37) as well as by Fourier transform infrared (FTIR) spectroscopy [38–40]. Furthermore, several well-resolved X-ray structures of the Q_A ground state are available [36, 41, 42]. Additionally, pulsed and high-field EPR spectroscopy on the light-induced radical pair $Q_A^{-\bullet}$-$P_{865}^{+\bullet}$ allowed to obtain structural information on the distance R, exchange coupling J [43] and the relative orientation of the dipolar axis R with respect to the $Q_A^{-\bullet}$ g-tensor axis system [44]. Due to the large amount of available experimental information, the $Q_A^{-\bullet}$ binding site is a good test system for quantum chemical calculations of EPR parameters. Such calculations might moreover be helpful to gain further insight into structural details of the Q_A binding site or into mechanisms leading to specific magnetic interactions.

So far, there are several theoretical studies on ubiquinone models which also relate to Q_A in bRCs of *Rhodobacter sphaeroides* [45–53]. Most of them [45,

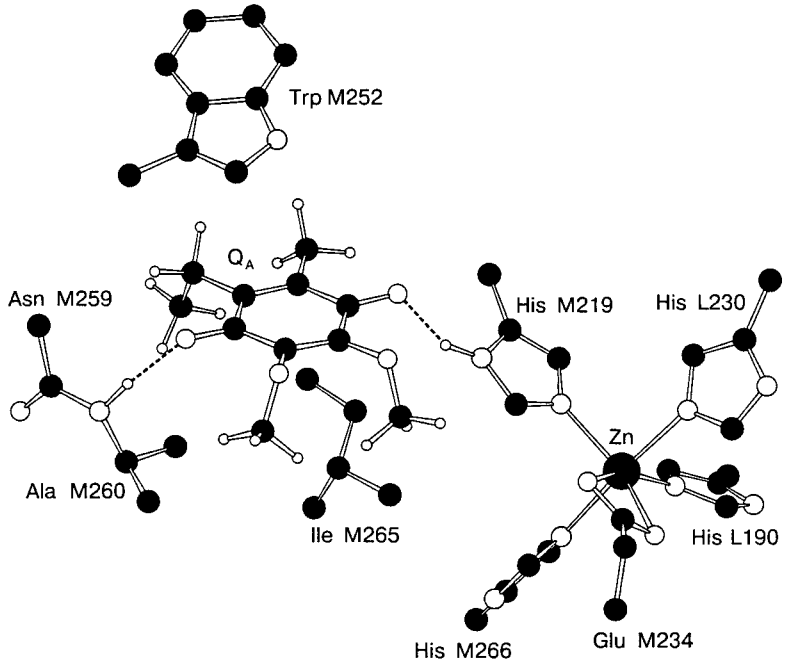

Fig. 1. Structure of the maximum-sized model of the $Q_A^{-\bullet}$ binding site (M4) as taken from crystal structure data and partially optimized. Only quinone and hydrogen bonded hydrogen atoms are shown. Residue labeling according to Stowell et al. [36].

47–49, 52, 53] also deal with EPR parameters, e.g., with the calculation of quinone HFC constants or electronic *g*-tensors. In this study unrestricted hybrid DFT is used to examine HFC and QC tensors as well as spin density distributions of various models of the $Q_A^{-\bullet}$ binding pocket. For all calculations the coordinates of Stowell et al. [36] at a resolution of 0.26 nm are employed as a starting point. The influence of several surrounding amino acids, a bivalent Zn^{2+} metal center[1] and geometry relaxation of the ubisemiquinone on the magnetic properties of the $Q_A^{-\bullet}$ binding site are discussed. The different models used in the present work take into account all short-range interactions of the quinone with the protein in a step-by-step manner. Despite the fact that already a number of quantum chemical calculations on $Q_A^{-\bullet}$ exist, we for the first time included all of these electronic, electrostatic and steric effects explicitly in a theoretical treatment of this system. Here, the major focus is put on the ^{14}N HFC and QC parameters of the two hydrogen bonding partners of the quinone, His219 and Ala260, as well as the orientation of $Q_A^{-\bullet}$ in its binding site.

---

[1] In the samples that are used to perform the EPR experiments the native paramagnetic Fe^{2+} is often substituted by the diamagnetic Zn^{2+} or just removed to avoid line broadening effects due to fast spin relaxation by the high-spin Fe^{2+}.

2 Theoretical Background and Computational Details

2.1 Hyperfine Coupling Tensor

The HFC tensor **A** expresses the interaction between unpaired electrons and magnetic nuclei N [54, 55]. It can be divided into an isotropic and an anisotropic (dipolar) part, A_{iso} and **T** respectively, according to

$$A_{ij}(N) = T_{ij}(N) + \delta_{ij} A_{iso}(N),$$

where δ_{ij} is the Kronecker delta and $i, j = x, y, z$. The isotropic HFC constants (HFCCs) correspond to the Fermi contact interactions and can in the first-order approximation (neglecting spin–orbit effects) be obtained via

$$A_{iso}(N) = \frac{4\pi}{3} \beta_e \beta_N g_e g_N \langle S_Z \rangle^{-1} \sum_{\mu,\nu} P_{\mu,\nu}^{\alpha-\beta} \langle \varphi_\mu | \delta(\mathbf{R}_N) | \varphi_\nu \rangle$$

with g_e and g_N as the electron and nuclear g-values, β_e and β_N as the Bohr and nuclear magneton, $\langle S_Z \rangle$ as the expectation value of the z component of the total electronic spin, $P_{\mu,\nu}^{\alpha-\beta}$ as the spin density matrix and $\mathbf{R}_N$ as the position vector of nucleus N. The summation runs over the atomic orbitals φ_i.

In the first-order approximation the components of the anisotropic tensor are given by

$$T_{ij}(N) = \frac{1}{2} \beta_e \beta_N g_e g_N \langle S_Z \rangle^{-1} \sum_{\mu,\nu} P_{\mu,\nu}^{\alpha-\beta} \langle \varphi_\mu | \mathbf{r}_N^{-5} (\mathbf{r}_N^2 \delta_{ij} - 3\mathbf{r}_{N,i} \mathbf{r}_{N,j}) | \varphi_\nu \rangle.$$

Here, $\mathbf{r}_N = \mathbf{r} - \mathbf{R}_N$ defines the position of the electron at $\mathbf{r}$ with respect to the nucleus N at $\mathbf{R}_N$.

2.2 Quadrupole Coupling Tensor

The QC tensor **Q** is a traceless tensor which describes the interaction of a nuclear electric quadrupole moment Q_N due to a nonspherical nuclear charge density (for $I > 1/2$) with the electric field of the surrounding electrons [56]. Its matrix elements are defined as [57]:

$$Q_{ij}(N) = \frac{eQ_N}{2I_N(2I_N - 1)h} V_{ij}(N),$$

where V_{ij} are the components of the electric field gradient (EFG) tensor. On the basis of the EFG tensor, one can define the QC constant (QCC) χ and the asymmetry parameter η as

$$\chi(N) = \frac{eQ_N V_{zz}(N)}{h}, \quad \text{and} \quad \eta(N) = \frac{V_{xx}(N) - V_{yy}(N)}{V_{zz}(N)}$$

with $|V_{zz}| \geq |V_{yy}| \geq |V_{xx}|$. The value of η lies between 0 and 1, and in case of axial symmetry, one obtains $|V_{xx}| = |V_{yy}|$ and $\eta = 0$. As the EFG tensor is traceless, χ and η are sufficient to fully describe the tensor in its principal axis system. For the calculations of the QCCs standard nuclear quadrupole moments of $Q_N(^{14}N) = 2.044(3)$ fm^2 as published by Tokman et al. [58] and $Q_N(^2H) = 0.2860(15)$ fm^2 as reported by Bishop and Cheung [59] (see also ref. 60) were used. As in many other studies [11, 12, 19, 27, 28] the nuclear quadrupole moments were not calibrated for the applied theoretical methods. Using the above mentioned values for Q_N it was possible to calculate the QCCs directly from the V_{zz} eigenvalues of the EFGs obtained from the computations.

2.3 Computational Details

All calculations in the present study were carried out using standard methods and basis sets as implemented in the Gaussian 98 [61] program package. All computations were done for the paramagnetic anion radical state of the quinone and using the unrestricted Kohn–Sham formalism or PM3 method. For calculations of HFC and EFG tensors a combination of Becke's three-parameter hybrid functional B3 [62] and of Perdew and Wang's correlation functional PW91 [63, 64] was applied together with the 6-31G(d) basis set in all cases. Tight SCF criteria and ultrafine integration grids were used in all property computations. Comparison with results from a calculation for one of the smaller models (M1, see below) employing the larger EPR-II basis set (data not shown) revealed that differences were usually below 10% except for the isotropic C-1/C-4 and O-1/O-4 HFC constants for which larger deviations were observed. Thus the choice of the 6-31G(d) basis set is justified, especially since a main focus of this work is set on the hydrogen-bound amino acid ligands. Partial geometry optimizations were performed using the semiempirical PM3 method [65, 66]. It has been shown previously that the use of PM3 geometries for HFC constant calculations leads to good results for hydrogen bonded semiquinone anion radicals [47, 67, 68].

2.4 Structural Models for $Q_A^{-\bullet}$ Binding Site

The different structural models of the quinone binding site consist of Q_A and several of the surrounding amino acid residues (see Table 1 and Fig. 1). The coordinates of all models were taken from the crystal structure of Stowell et al. [36] and hydrogen atoms were added using standard bond lengths and angles. The isoprenoid side chain of Q_A was shortened to yield a C_2 alkyl chain. With these structures as starting points, partial optimizations of selected atoms were performed. In the smallest model (M1) only Q_A and the directly hydrogen bonded amino acids His219 and Ala260 (in conjunction with parts from Asn259) were taken into account. In models M2 and M3a/b the residues Trp252 and Ile265 were included, respectively, to consider electronic π–π interactions as well as steric constraints for Q_A. M3a

Table 1. Overview of the different structural models of the $Q_A^{-\bullet}$ binding site from bRCs of *R. sphaeroides* (M1–M4) as employed in the calculations. All amino acids are from the M chain unless otherwise denoted.

Model	Residues
M1	$Q_A^{-\bullet}$ + His219 + Ala260[a]
M2	$Q_A^{-\bullet}$ + His219 + Ala260[a] + Trp252
M3a/b	$Q_A^{-\bullet}$ + His219 + Ala260[a] + Trp252 + Ile265
M4	$Q_A^{-\bullet}$ + His219 + Ala260[a] + Trp252 + Ile265 + Zn^{2+} and ligands[b]

[a] In conjunction with parts from Asn259.
[b] Glu234 and His266 from the M chain and His190 and His230 from the L chain.

represents a well-defined model of the binding pocket and can therefore be used for a full geometry optimization of the quinone within the fixed amino acid framework (leading to M3b). Finally in model M4 the non-heme Fe^{2+} ion (which is directly coordinated to His219) from the crystal structure was replaced by Zn^{2+} and added together with its first ligand sphere (His190 and His230 from the L chain and Glu234 and His266 from the M chain; see Fig. 1). Inclusion of all metal ligands is important for a correct description of the charge distribution and thus especially for a correct prediction of the EFG tensors. It should be briefly mentioned that the role of the Zn^{2+} ion has previously been discussed in the context of C-1/C-4 and O-1/O-4 HFC tensors by O'Malley [52]. The structural models were chosen to account for all short-range interactions with the immediate protein surroundings, such as hydrogen bonding as well as steric, electronic and electrostatic interactions, in a successive way.

In all models some of the amino acid backbone or sidechain atoms were neglected according to Fig. 1 to keep the computational models as simple as possible. Table 1 shows an overview of the various models for the $Q_A^{-\bullet}$ binding site and Fig. 2 explains the nomenclature used in this work to distinguish between the different interacting magnetic nuclei.

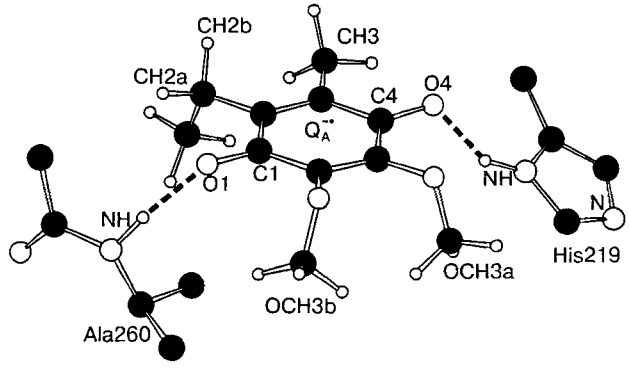

Fig. 2. Definition of the atom labeling scheme for the $Q_A^{-\bullet}$ binding site. Only quinone and hydrogen-bonded hydrogen atoms are shown.

3 Results and Discussion

The EPR properties of the binding site models for $Q_A^{-\bullet}$ from bRCs of *Rhodobacter sphaeroides* are investigated by comparing the results for the different geometric models described above (M1–M4). The influence of the various surrounding amino acids on the magnetic resonance parameters and the relation of the theoretical parameters to experimental values as well as the implications for the structure of the

Table 2. Theoretical $Q_A^{-\bullet}$ EPR parameters for various models of the $Q_A^{-\bullet}$ binding site from bRCs of *R. sphaeroides* (M1–M4) as calculated on the UB3PW91/6-31G(d)//UPM3 level of theory and comparison with experimental data. All HFC and QC constants are in MHz.

Parameter	M1[a]	M2[a]	M3a[a]	M3b[b]	M4[b]	Exp.[c]
$A_{iso}(^{13}C1)$	+2.57	+2.72	+2.55	+4.43	+2.28	(−)1.5(13)
$A_{xx}(^{13}C1)$	−7.76	−7.75	−7.87	−6.45	−7.78	(−)12.6(17)
$A_{yy}(^{13}C1)$	−3.88	−3.86	−3.99	−2.81	−3.97	(−)14.6(17)
$A_{zz}(^{13}C1)$	+19.34	+19.77	+19.51	+22.55	+18.59	(+)22.7(6)
$A_{iso}(^{13}C4)$	+9.01	+8.99	+7.57	+7.68	+11.41	(+)5.3(13)
$A_{xx}(^{13}C4)$	−3.64	−3.53	−4.33	−4.47	−2.35	(−)9.2(17)
$A_{yy}(^{13}C4)$	−0.48	−0.36	−1.14	−1.17	+0.66	(−)9.8(17)
$A_{zz}(^{13}C4)$	+31.15	+30.85	+28.18	+28.69	+35.92	(+)35.0(6)
$A_{iso}(^{17}O1)$	−23.41	−23.32	−22.76	−21.59	−22.04	—
$A_{xx}(^{17}O1)$	+12.94	+13.09	+13.64	+13.31	+13.68	—
$A_{yy}(^{17}O1)$	+12.39	+12.54	+13.07	+12.76	+13.15	—
$A_{zz}(^{17}O1)$	−95.56	−95.59	−94.99	−90.84	−92.95	(−)94(1)
$A_{iso}(^{17}O4)$	−19.09	−19.04	−19.63	−20.82	−21.07	—
$A_{xx}(^{17}O4)$	+12.44	+12.38	+12.23	+12.19	+10.47	—
$A_{yy}(^{17}O4)$	+11.93	+11.86	+11.67	+11.67	+9.86	—
$A_{zz}(^{17}O4)$	−81.64	−81.35	−82.79	−86.33	−83.54	(−)75(1)
$A_{iso}(^{1}H_{CH3})$[d]	+3.25	+2.75	+3.83	+4.90	+3.47	(+)4.5(2)
$A_{xx}(^{1}H_{CH3})$[d]	+1.50	+1.04	+2.06	+3.24	+1.86	(+)3.2(2)
$A_{yy}(^{1}H_{CH3})$[d]	+2.44	+1.99	+2.95	+4.04	+2.65	(+)3.6(2)
$A_{zz}(^{1}H_{CH3})$[d]	+5.82	+5.23	+6.49	+7.42	+5.91	(+)6.8(2)
$A_{iso}(^{1}H_{CH2a})$	+0.81	+0.75	+0.25	+0.89	+0.86	—
$A_{xx}(^{1}H_{CH2a})$	−1.55	−1.60	−2.12	−1.33	−1.36	—
$A_{yy}(^{1}H_{CH2a})$	−0.41	−0.49	−1.01	−0.24	−0.28	—
$A_{zz}(^{1}H_{CH2a})$	+4.39	+4.34	+3.88	+4.24	+4.22	—
$A_{iso}(^{1}H_{CH2b})$	+4.32	+4.34	+4.99	+4.60	+5.79	(+)6.4(2)
$A_{xx}(^{1}H_{CH2b})$	+2.70	+2.74	+3.43	+3.16	+4.36	(+)5.0(2)
$A_{yy}(^{1}H_{CH2b})$	+3.48	+3.47	+4.16	+3.89	+5.03	(+)5.6(2)
$A_{zz}(^{1}H_{CH2b})$	+6.77	+6.81	+7.38	+6.75	+7.99	(+)8.6(2)

[a] Only hydrogen bond atoms C, O, H and N were optimized.

[b] $Q_A^{-\bullet}$ and hydrogen bond NH groups optimized.

[c] See ref. 35 and references therein as well as ref. 76.

[d] The ^1H hyperfine couplings of the quinone methyl group were calculated by averaging the values for all three hydrogen atoms ($A = (A_1 + A_2 + A_3)/3$), i.e., assuming a rapid rotation of the methyl group under experimental conditions. This procedure has been successfully applied previously by Eriksson et al. [77], but see also ref. 78 for a critical discussion.

binding site are discussed. Furthermore, the amino nitrogen quadrupole parameters of His219 are related to the hydrogen bond geometry.

Tables 2 and 3 show the computed EPR parameters for the various models (M1–M4) of the $Q_A^{-\bullet}$ binding site. The EPR parameters were calculated on the B3PW91/6-31G(d) level using PM3-optimized geometries. In some of the partial geometry optimizations (M1–M3a) only the CO···HN hydrogen bond atoms on both sides of the semiquinone were optimized, while the rest of the structure was kept fixed, and in other computations (M3b and M4) the whole semiquinone and the NH groups of the hydrogen bonded amino acids His219 and Ala260 were able to freely rearrange within the fixed frame of the surrounding residues defining the binding pocket.

Table 3. Theoretical His219 and Ala260 EPR parameters for various models of the $Q_A^{-\bullet}$ binding site from bRCs of *R. sphaeroides* (M1–M4) as calculated on the UB3PW91/6-31G(d)//UPM3 level of theory and comparison with experimental data. All HFC and QC constants are in MHz.

Residues	Parameter	M1[a]	M2[a]	M3a[a]	M3b[b]	M4[b]	Exp.[c]
His219	$\chi(^{14}N_{NH})$	+1.889	+1.911	+1.914	+1.914	+1.506	(+)1.65(5)
	$\eta(^{14}N_{NH})$	0.342	0.317	0.286	0.297	0.649	0.73
	$\chi(^{14}N_{N})$	+4.332	+4.337	+4.253	+4.250	+2.360	—
	$\eta(^{14}N_{N})$	0.061	0.063	0.081	0.076	0.363	—
	$\chi(^{2}H_{NH})$	−0.222	−0.223	−0.221	−0.227	−0.196	(−)0.168
	$\eta(^{2}H_{NH})$	0.135	0.135	0.125	0.128	0.121	0.024
	$A_{iso}(^{14}N_{NH})$	+2.63	+2.55	+2.44	+2.66	+2.44	~2
	$A_{xx}(^{14}N_{NH})$	+2.31	+2.23	+2.14	+2.35	+2.19	~1.8
	$A_{yy}(^{14}N_{NH})$	+2.36	+2.28	+2.19	+2.40	+2.23	~1.8
	$A_{zz}(^{14}N_{NH})$	+3.22	+3.14	+2.99	+3.24	+2.91	~2.4
	$A_{iso}(^{1}H_{NH})$	−0.87	−0.96	−1.10	−0.92	−0.06	(−)1.2
	$A_{xx}(^{1}H_{NH})$	−6.41	−6.46	−6.32	−6.35	−5.22	(−)6.4
	$A_{yy}(^{1}H_{NH})$	−5.88	−5.92	−5.90	−6.00	−4.78	(−)6.4
	$A_{zz}(^{1}H_{NH})$	+9.69	+9.49	+8.93	+9.59	+9.82	(+)9.1
Ala260	$\chi(^{14}N_{NH})$	+3.307	+3.320	+3.422	+3.413	+3.491	(+)3.05(5)
	$\eta(^{14}N_{NH})$	0.291	0.281	0.437	0.424	0.387	0.54
	$\chi(^{2}H_{NH})$	−0.207	−0.209	−0.211	−0.213	−0.218	(−)0.202
	$\eta(^{2}H_{NH})$	0.218	0.216	0.223	0.210	0.206	0.386
	$A_{iso}(^{14}N_{NH})$	−0.05	−0.09	+0.20	+1.38	+1.09	~2
	$A_{xx}(^{14}N_{NH})$	−0.23	−0.26	−0.05	+1.09	+0.82	~1.8
	$A_{yy}(^{14}N_{NH})$	−0.21	−0.24	−0.03	+1.11	+0.83	~1.8
	$A_{zz}(^{14}N_{NH})$	+0.28	+0.24	+0.68	+1.94	+1.62	~2.4
	$A_{iso}(^{1}H_{NH})$	−0.44	−0.39	−0.81	−1.57	−1.49	(−)0.2
	$A_{xx}(^{1}H_{NH})$	−4.09	−4.02	−4.64	−6.59	−6.28	(−)4.8
	$A_{yy}(^{1}H_{NH})$	−3.90	−3.82	−4.46	−6.23	−5.92	(−)4.8
	$A_{zz}(^{1}H_{NH})$	+6.67	+6.67	+6.67	+8.11	+7.73	(+)9.1

[a] Only hydrogen bond atoms C, O, H and N were optimized.
[b] $Q_A^{-\bullet}$ and hydrogen bond NH groups optimized.
[c] See ref. 35 and references therein as well as refs. 37 and 73.

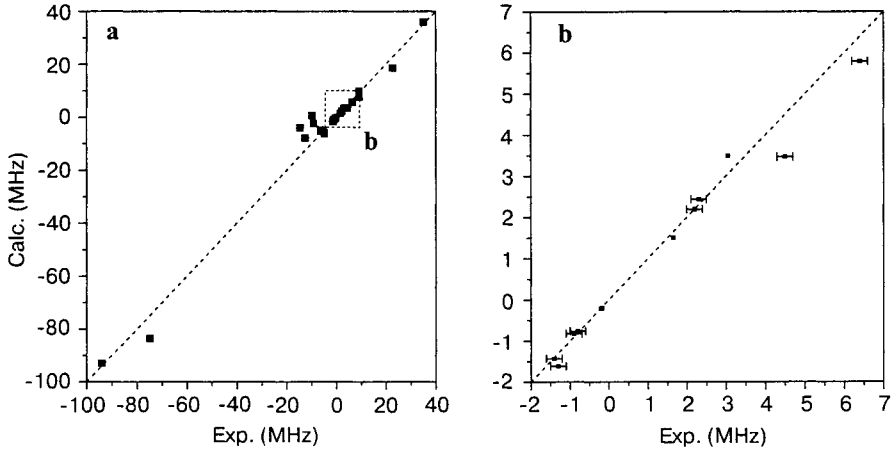

Fig. 3. Correlation between experimental (for references see Tables 2 and 3) and calculated EPR parameters of the $Q_A^{-\cdot}$ binding site. The theoretical values for the HFCCs and QCCs were taken from the computation for model M4. The total range of coupling constants is shown in **a**, whereas **b** depicts a magnification of the area from −2 to +7 MHz. All values are in megahertz and for some of the experimental data error bars are shown in **b**. The dashed line represents the ideal correlation.

Before drawing any conclusions from the calculations, a comparison of these results with experimental data is required to prove the reliability of the computational methods and demonstrate that such theoretical predictions are feasible for complex biological systems using rather small structural models. A good correlation between experiment and theory as depicted in Fig. 3 is obtained. This graph includes all experimental values from Table 2, the QCCs and ^{1}H HFCCs from Table 3 and the theoretical values from model M4 which should be the most realistic model of the $Q_A^{-\cdot}$ binding site. Most of the computed values lie within a 15% range around the corresponding experimental values.

A comparison of the results of the computations for the models M1–M3a reveals that the inclusion of Trp252 and Ile265 does not dramatically influence the HFC or QC parameters of the semiquinone or its directly bound ligands.[2] Only the rather sensitive asymmetry parameters of the nitrogen atoms of the NH groups of His219 and Ala260 as well as some components of the ^{13}C4, ^{17}O4, methyl and methylene HFC tensors change slightly, especially when introducing Ile265. Much larger alterations of EPR parameters are observed when going to the optimized structure of M3b or particularly when including the Zn^{2+} ion with its ligands in M4. The most interesting changes on which we focus here concern the nitrogens of the hydrogen-bonded amino acid residues. One major difference in the EPR parameters of the optimized models (M3b and M4) compared to M1–M3a is the value of the isotropic ^{14}N HFCC of the Ala260 backbone

[2] For an investigation of quinone–tryptophan interactions and the implications for the energetics and the electronic *g*-tensors of such systems see, e.g., ref. 69.

nitrogen ($A_{iso}(^{14}N_{NH})$) which changes from +0.20 (M3a) to +1.38 (M3b) or +1.09 MHz (M4). This increase of spin density on the alanine nitrogen can be understood when comparing the different optimized structures. Figure 4 visualizes the rearrangement of the semiquinone within its binding pocket upon geometry optimization for M4. $Q_A^{-\bullet}$ mainly rotates in the quinone plane which leads to a slight elongation of the N–O distance and a slight shortening of the H–O distance at the Ala260 site (Table 4). The structure at the His219 site does not change significantly. Therefore, the overall effect of the reorientation is a linearization of the hydrogen bonds, i.e., of the N–H···O sequence of atoms, especially for the alanine hydrogen bond. This linearization enables a more efficient orbital overlap and therefore an increased transfer of spin density from the quinone to the ligand nitrogens leading to larger isotropic HFCCs in good agreement with the experimental data.

In line with the observation that there is a structural difference between the neutral and radical anion state, Sinnecker et al. [19] have also found that the hydrogen bond between a benzoquinone and a water gets shorter by about 0.025 nm upon formation of the radical anion. This might in general be of importance for comparison of calculation on the paramagnetic quinone state with crystal structure data that often involve diamagnetic quinones.

It should be mentioned that the optimized orientation of the semiquinone molecule in model M4 leads to a better agreement with the fit of the W-band correlated-coupled radical pair spectra of $Q_A^{-\bullet}$-$P_{865}^{+\bullet}$ [44] compared to the X-ray structure data. The low-field part of the spin-polarized spectra is determined solely by the length as well as orientation of the interconnecting vector **R** between $Q_A^{-\bullet}$ and $P_{865}^{+\bullet}$ with respect to the quinone *g*-tensor axis system, assuming a negligible exchange interaction between them [43, 70]. The optimum fit values for the polar angles of the **R** vector in the quinone *g*-tensor axis system are $\theta = 79.4°$ and $\varphi = 62.3°$, whereas the M4 geometry-optimized values are $\theta = 81.1°$ and $\varphi = 56.7°$, compared to the original values from the X-ray structure [36] of $\theta = 74.8°$ and $\varphi = 72.4°$.

Model M4 was also chosen to account for effects due to the positive charges of the divalent zinc ion. Here, a shortening of the N–O and the H–O distance at the His219 site compared to M3b (Table 4), i.e., a stronger interaction between

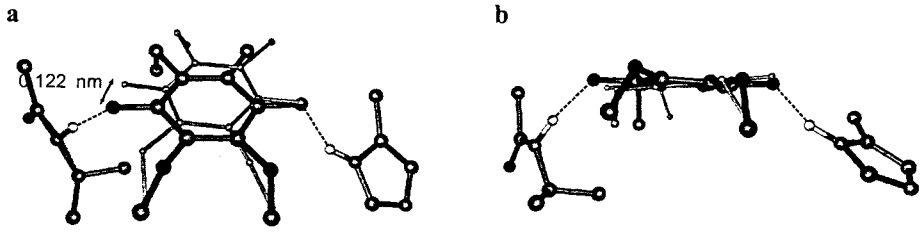

Fig. 4. Rearrangement of $Q_A^{-\bullet}$ upon partial geometry optimization (PM3) from a top (**a**) and side view (**b**). The optimized structure (M4) is shown in a grayscale ball and stick representation, the crystal structure in a thin one-color ball and stick representation. Most hydrogen atoms, Trp252, Ile265 and Zn^{2+} with further ligands are omitted for clarity.

Table 4. Important geometric hydrogen bond parameters for various models of the $Q_A^{-\bullet}$ binding site from bRCs of *R. sphaeroides* (M1–M4) as calculated on the UPM3 level of theory and comparison with crystallographic data. Bond lengths are in nanometers.

Bond length	M1[a]	M2[a]	M3a[a]	M3b[b]	M4[b]	Crystal[c]
$r(N_{His}–O4)$	0.272	0.273	0.271	0.273	0.266	0.291
$r(H_{His}–O4)$	0.175	0.176	0.177	0.177	0.171	—
$r(N_{Ala}–O1)$	0.279	0.278	0.277	0.282	0.284	0.283
$r(H_{Ala}–O1)$	0.184	0.184	0.184	0.180	0.182	—

[a] Only hydrogen bond atoms C, O, H and N were optimized.
[b] $Q_A^{-\bullet}$ and hydrogen bond NH groups optimized.
[c] From ref. 36.

$Q_A^{-\bullet}$ and its ligand, is observed. Due to this rearrangement the distance between the semiquinone and Ala260 slightly increases and the corresponding isotropic HFCC of the alanine nitrogen slightly reduces. However, even though there are no major structural changes when going from M3b to M4, large changes of the quadrupole parameters of the His219 nitrogen atoms are observed. The QCC of the amino nitrogen $\chi(^{14}N_{NH})$ decreases from +1.914 (M3b) to +1.506 MHz (M4) and the one of the imino nitrogen ($\chi(^{14}N_N)$) even from +4.250 (M3b) to +2.360 MHz (M4). The asymmetry parameters $\eta(^{14}N_{HN,N})$ increase from 0.297 to 0.649 and from 0.076 to 0.363, respectively. Altogether these changes lead to a better agreement with experimental data for M4. As a conclusion, it is possible to say that Trp252 and Ile265 do not significantly influence the HFC and QC parameters of the $Q_A^{-\bullet}$ site but they are necessary to define the binding pocket in further calculations where the semiquinone is allowed to rearrange. However, this structural reorientation together with the influence of the Zn^{2+} ion significantly alter certain EPR parameters of the hydrogen-bonded amino acid residues His219 and Ala260.

In order to further disentangle direct (electrostatic or electronic) influences of the zinc ion and indirect influences due to structural changes induced in M4, an EPR parameter calculation was performed for a model system based on the optimized geometry M4 but where the Zn^{2+} and its ligands (except His219) were deleted. The structure of this model was not optimized again. Without including the divalent metal explicitly, the QC parameters of His219 were computed to be $\chi(^{14}N_{NH}) = +1.808$ and $\eta(^{14}N_{NH}) = 0.393$ as well as $\chi(^{14}N_N) = +4.249$ and $\eta(^{14}N_N) = 0.067$ for the amino and imino nitrogens, respectively. A comparison of these results with the QC parameters of the models M3b and M4 (see Table 3) indicates that structural changes like the shortening of the $N_{His}–O4$ distance (Table 4) as well as direct effects of the metal ion are important to reproduce the QC parameters of His219. When going from M3b to the truncated M4 model, the amino QC constant slightly decreases and the asymmetry parameter increases, whereas the imino QC parameters remain virtually constant. These influences due to structural changes are considerably smaller than those of the Zn^{2+} itself.

When going from the modified M4 model to M4, the amino and the imino QC constants decrease and the asymmetry parameters increase. In summary, these results reveal a pronounced direct influence of the zinc ion on the His219 QC parameters (see also the discussion of metal influence below).

One important point that is discussed in depth in the experimental literature is the strength of the two hydrogen bonds of $Q_A^{-\bullet}$ [35]. The formation of a hydrogen bond to one of the carbonyl oxygens of the semiquinone anion radical leads to a shift of spin density and charges within the semiquinone ring. The bound oxygen will possess a larger negative charge to stabilize the hydrogen bonding interaction and thus the spin density will partly be shifted within the semiquinone. When two hydrogen bonds, one at each carbonyl oxygen of the semiquinone, are present, there will be competing mechanisms shifting spin density and charges. In that case the dominating effect will be due to the stronger one of the two hydrogen bonds, i.e., the carbonyl oxygen involved in the stronger bond will possess a larger negative charge than the other and the spin density will partly be shifted to the opposite side of the semiquinone. Figure 5a depicts this schematically for the $Q_A^{-\bullet}$ binding site assuming a stronger hydrogen bond to His219. Here, the negative charge is localized at the carbonyl oxygen coordinated to the histidine ligand indicating a stabilized bond and the mesomeric structures visualize the increase of spin density at the opposite side of the ring system. Experimental data show that this is exactly the situation in the $Q_A^{-\bullet}$ pocket and that the hydrogen bond to His219 is slightly stronger than that to Ala260 [35].

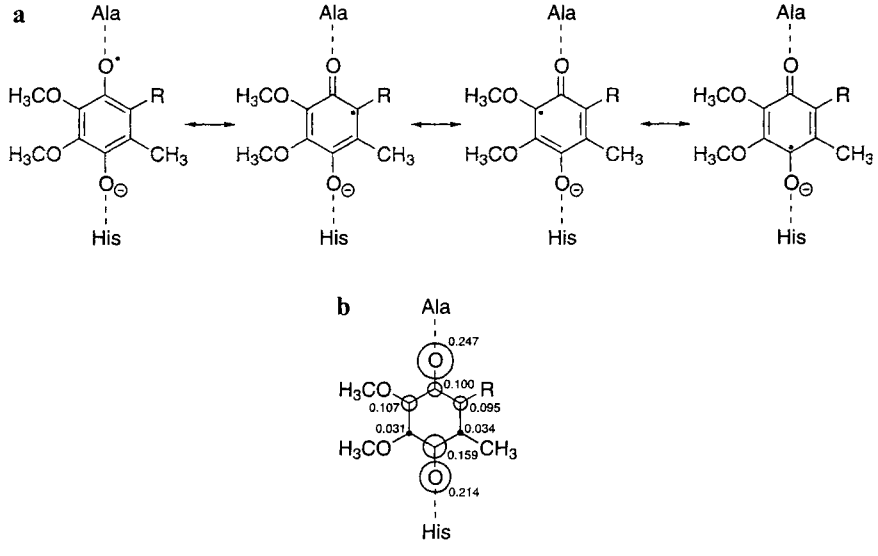

Fig. 5. **a** Simple valence bond model to explain the charge and spin density distribution of $Q_A^{-\bullet}$ in its binding pocket. Energetically favored mesomeric structures are shown for the case of a stronger hydrogen bond interaction to His. **b** Schematic representation of the total atomic spin densities (in a.u.) from a Mulliken population analysis for model M4.

A comparison of this experimental prediction with the calculations for model M4 exhibits a very good agreement. The Mulliken population analysis yields a slightly larger negative charge for O-4 (−0.67 a.u.) than for O-1 (−0.61 a.u.) and a total atomic spin density distribution schematically presented in Fig. 5b. The spin density at O-1 is larger than at O-4, at C-4 it is larger than at C-1, and at C-2 and C-6 the spin density is larger than at C-3 and C-5. This asymmetric charge and spin density distribution corresponds to mesomeric structures as shown in Fig. 5a revealing a stronger hydrogen bonding interaction to the His219 residue in perfect accordance with the experimental results and a previous theoretical study [52].

On the basis of this convincing agreement between theory and experiment it is possible to use quantum chemistry to interpret EPR spectroscopical data for this system and correlate it to molecular structure. From 3-pulse ESEEM measurements of Lendzian et al. [71] and Spoyalov et al. [72] it is known that the unpaired electron of the $Q_A^{-\bullet}$ semiquinone anion radical interacts with two different nitrogen nuclei which were assigned to the backbone nitrogen of Ala260 and the amino nitrogen of His219. For both nitrogens the QC parameters could be extracted from the corresponding ν_0, ν_+ and ν_- frequency sets of one-electron spin manifold when assuming the validity of the exact cancellation condition [2] for this manifold. To fulfill this condition and thus get sharp lines in the frequency domain ESEEM spectra, there has to be a certain amount of spin density at the positions of the nuclei which corresponds to isotropic ^{14}N HFCCs of about 2 MHz. However, no exact specification of the size of these couplings could be given because only one double quantum frequency ν_{dq} of the other electron spin manifold for one nitrogen was observed in the frequency domain 3-pulse ESEEM spectra. Furthermore, this frequency could not be assigned to one of the two nitrogen nuclei. To gain further experimental information about the isotropic HFCCs, simulations of the 3-pulse ESEEM measurements would be necessary. Additionally, two-dimensional correlation experiments such as HYSCORE would be needed to assign the double quantum peak of the second electron spin manifold at ν_{dq} to the corresponding characteristic ν_0, ν_+ and ν_- frequencies.

When looking at the computational results of model M3a (without Q_A rearrangement) one finds for $A_{iso}(^{14}N_{NH})$ of His219 a value of +2.44 MHz and for Ala260 a value of +0.20 MHz. The Ala260 HFCC is much smaller than the experimental value of ca. 2 MHz, i.e., the structure used for the computations does not reflect the experimental data. In contrast to that, the calculations with the optimized orientations of $Q_A^{-\bullet}$ yield larger isotropic couplings for the alanine nitrogen of +1.38 (M3b) and +1.09 MHz (M4) that are closer to the experimental estimation. The HFCCs for the histidine amino nitrogen do not change significantly for M3b (+2.66 MHz) and M4 (+2.44 MHz). These theoretical data indicate that the binding site geometry of the $Q_A^{-\bullet}$ anion radical state accessible via EPR spectroscopy is slightly altered with respect to the geometry of the Q_A ground state as investigated by X-ray crystallography as a structural reorientation is necessary to predict HFCCs that fit the experimental data. However, it should be noted that the rearrangement is only slightly larger than the estimated

error in atomic positions of roughly 0.09 nm (one third of the crystal structure resolution) for the crystal structure. Besides yielding this structural information, the calculations also help to assign the double quantum frequency ν_{dq} observable in the 3-pulse ESEEM spectra to a specific nitrogen. Assuming that ν_{dq} belongs to His219 or Ala260, it is possible to calculate the corresponding isotropic HFCCs for these two hypothetical cases: +1.8 or +1.1 MHz, respectively [72]. A comparison of these values with the computed couplings of +2.44 MHz for His219 and +1.09 MHz for Ala260 reveals that the hypothetical value for alanine comes closer to the corresponding theoretical coupling value than for histidine. Therefore, it can be suggested that the observed double quantum peak belongs to the Ala260 backbone nitrogen.

A comparison of the QC parameters of the hydrogen-bonded nitrogens of His219 and Ala260 from the models M3b and M4 with the values from ESEEM spectroscopy shows very good agreement for M4. Concerning M3b, only both QCCs and the asymmetry parameter of Ala260 show good agreement, whereas the asymmetry parameter of the His219 amino nitrogen (0.297) deviates significantly from the experimental value (0.73). Therefore, the influence from the divalent metal ion (Zn^{2+}) which strongly alters this parameter are required for a correct description of the electronic situation at the His219 site (see also the discussion of metal influence above and below). Again, the excellent agreement between theory (M4) and experiment allows a correlation between spectroscopic data and molecular structure.

The ^2H QC parameters of the hydrogen bonds (Table 3) are rather insensitive to any of the applied changes of the molecular geometry or the model size. For M4 one obtains for the ^2H from the NH of His219 a χ of -0.196 MHz and a η of 0.121 and for Ala260 a χ of -0.218 MHz and a η of 0.206 in good agreement with the experimental values [73]. The ^1H HFC tensors of the hydrogen bonds are strongly anisotropic and the isotropic HFCCs have negative signs, i.e., the spin density at the corresponding nuclei is due to spin polarization effects. In the literature there are different interpretations concerning the detectable ^1H ENDOR frequencies [35, 74]. A very recent study using differing exchange times for D_2O now has conclusively assigned the HFCCs from exchangeable protons [37]. The results obtained and their assignments (see Table 3) agree well with those predicted by our computational results.

Finally, we are going to discuss the calculated ^{14}N QC parameters of His219 in the context of the hydrogen bond geometry and compare these data with results of systematic studies described for the imidazole–water and methylimidazole-benzosemiquinone systems in ref. 75.

First of all, the models M1–M3a/b are considered because the QC parameters of the amino and imino nitrogens of His219 are very similar for all of these models. For the imino nitrogen, the QCC as well as the asymmetry parameter are similar to those of free histidine (QC parameters for a free methylimidazole with a structure as in model M4: $\chi = 2.740$ MHz and $\eta = 0.431$ as well as $\chi = 4.314$ MHz and $\eta = 0.113$ for the amino and imino nitrogens, respectively) but for the amino nitrogen $\chi = +1.914$ MHz (for M3b) is smaller than for free histidine.[3]

According to the results for the methylimidazole-benzosemiquinone system, this indicates a hydrogen bonding interaction to the amino group with a hydrogen bond length shorter than about 0.3 nm. Table 4 shows that this is indeed true as the O–N distance ranges from 0.271 to 0.273 nm for M1–M3b.

However, when moving on to M4, the situation becomes more complicated by the additional His219–Zn^{2+} interaction. Such effects have not been included in the systematic studies and render an analysis much more difficult. In this case also the imino QC parameters deviate significantly from the free values due to the altered electric field gradient at this atomic position. For the amino nitrogen the QCC is even a bit smaller than for the other three models but the asymmetry parameter is much larger than before and also larger than the free value. Following the systematic trends [75] this would suggest a considerably shortened hydrogen bond. However, this is not the case since the bond length decreases by only about 0.006 nm compared to M1–M3a/b. Such a small change cannot fully account for the dramatic increase of η (see also above for a discussion about direct and indirect influences of the metal). Therefore, in that case effects other than just the hydrogen bond geometry might have an influence on the QC parameters and the simple rules from the systematic studies might not be sufficient to completely describe the quadrupole interaction. It should be noted that it cannot be excluded on the basis of the present computations that part of this increase of the asymmetry parameter may be due to the slightly distorted ring geometry around the amino nitrogen as taken from the crystal structure. Another important point to notice is that the metal ion considerably alters the imino nitrogen parameters, the QC constant decreases and the asymmetry parameter increases upon inclusion of Zn^{2+} and its ligands.

4 Conclusions

For the $Q_A^{-\bullet}$ binding site from bRCs of *Rhodobacter sphaeroides* it was demonstrated by correlation with experimental data that theoretical studies of EPR parameters and spin density distributions on such complex biological systems are feasible and yield reliable results. On the basis of this convincing agreement between theory and experiment, the computational results were used to extend the interpretation of existing spectroscopic data and correlate these data with molecular structure. Furthermore, the different specific semiquinone–protein interactions and their influence on the EPR parameters of the binding pocket were analyzed in detail by using structural models that include these interactions step by step.

The selected strategy of comparing experimentally estimated and calculated isotropic ^{14}N HFCCs of the hydrogen bonded His219 and Ala260 residues for

---

[3] It should be noted that the fact that the asymmetry parameter of $\eta = 0.297$ (for M3b) is smaller than for the free methylimidazole is due to the slightly distorted structure of the five-membered ring as taken from the crystal structure. It does thus not reflect a systematic behavior as described in ref. 75 but can to some extent be considered as an artefact caused by the structural model.

different structural models led to new information about the orientation of $Q_A^{-\bullet}$ in the binding site and indicated that the binding site geometry of the $Q_A^{-\bullet}$ anion radical state is slightly altered with respect to the crystal structure of the Q_A ground state. This structural reorientation upon geometry optimization as well as the inclusion of the divalent metal ion significantly influence certain EPR parameters of the hydrogen bonded amino acid residues His219 and Ala260 and are necessary to fit the experimental data. Moreover, the slight reorientation of the semiquinone molecule in model M4 is in agreement with W-band correlated-coupled radical pair spectra of $Q_A^{-\bullet}$-$P_{865}^{+\bullet}$ [44]. The orientation of the dipolar vector **R** with respect to the $Q_A^{-\bullet}$ *g*-tensor axis system of this structure is in better agreement with the obtained optimal fit values than the X-ray structure orientation data. In addition to this structural information, the computations also allowed us to suggest an assignment of the observed double quantum frequency from 3-pulse ESEEM spectra to the Ala260 backbone nitrogen.

In conclusion, it was possible in this study to successfully employ DFT calculations of EPR parameters to gain more insight into the structure and properties of $Q_A^{-\bullet}$ and its binding environment in bRCs.

Acknowledgments

This work was financially supported by the DFG (Sfb 472, Molecular Bioenergetics). J.F. gratefully acknowledges support by the Fonds der Chemischen Industrie (Chemiefondsstipendium für Doktoranden) and by the Frankfurt Center for Scientific Computing. We thank W. Lubitz for providing experimental ^{2}H QC data prior to publication. Thanks to S. Grimaldi (Univ. Marseille) for personal discussions.

References

1. Weil J.A., Bolton J.R., Wertz J.E.: Electron Paramagnetic Resonance: Elementary Theory and Practical Applications. New York: Wiley 1994.
2. Schweiger A., Jeschke G.: Principles of Pulse Electron Paramagnetic Resonance. Oxford: Oxford University Press 2001.
3. Parr R.G., Yang W.: Density-Functional Theory of Atoms and Molecules. New York: Oxford University Press 1989.
4. Engels B., Eriksson L.A., Lunell S.: Adv. Quantum Chem. **27**, 297–369 (1996)
5. Barone V., in: Recent Advances in Density Functional Methods, Part I (Chong D.P., ed.). Singapore: World Scientific Press 1996.
6. Malkin V.G., Malkina O.L., Eriksson L.A., Salahub D.R., in: Modern Density Functional Theory: A Tool for Chemistry (Seminario J.M., Politzer P., eds.). Amsterdam: Elsevier 1995.
7. Kaupp M., Malkin V.G., Bühl M. (eds.): Calculation of NMR and EPR Parameters. Weinheim: Wiley-VCH 2004.
8. Munzarová M., Kaupp M.: J. Phys. Chem. A **103**, 9966–9983 (1999)
9. Neese F.: Curr. Opin. Chem. Biol. **7**, 125–135 (2003)
10. Sinnecker S., Neese F., Noodleman L., Lubitz W.: J. Am. Chem. Soc. **126**, 2613–2622 (2004)
11. Koster A.M., Calaminici P., Russo N.: Phys. Rev. A **53**, 3865–3868 (1996)
12. Salzmann R., Kaupp M., McMahon M.T., Oldfield E.: J. Am. Chem. Soc. **120**, 4771–4783 (1998)

13. de Luca G., Russo N., Köster A.M., Calaminici P., Jug K.: Mol. Phys. **97**, 347–354 (1999)
14. Bailey W.C.: Chem. Phys. **252**, 57–66 (2000)
15. Sicilia E., de Luca G., Chiodo S., Russo N., Calaminici P., Köster A.M., Jug K.: Mol. Phys. **99**, 1039–1051 (2001)
16. Janowski T., Jaszunski M.: Int. J. Quantum Chem. **90**, 1083–1090 (2002)
17. Latosińska J.N.: Int. J. Quantum Chem. **91**, 284–296 (2003)
18. Zhang Y., Gossman W., Oldfield E.: J. Am. Chem. Soc. **125**, 16387–16396 (2003)
19. Sinnecker S., Reijerse E., Neese F., Lubitz W.: J. Am. Chem. Soc. **126**, 3280–3290 (2004)
20. Stein M., van Lenthe E., Baerends E.J., Lubitz W.: J. Am. Chem. Soc. **123**, 5839–5840 (2001)
21. Stein M., Lubitz W.: Phys. Chem. Chem. Phys. **3**, 2668–2675 (2001)
22. Wetmore S.D., Smith D.M., Golding B.T., Radom L.: J. Am. Chem. Soc. **123**, 7963–7972 (2001)
23. O'Malley P., Collins S.J.: J. Am. Chem. Soc. **123**, 11042–11046 (2001)
24. Sinnecker S., Koch W., Lubitz W.: J. Phys. Chem. B **106**, 5281–5288 (2002)
25. Jaszewski A.R., Jezierska J.: Chem. Phys. Lett. **343**, 571–580 (2001)
26. van Gastel M., Coremans J.W.A., Sommerdijk H., van Hemert M.C., Groenen E.J.J.: J. Am. Chem. Soc. **124**, 2035–2041 (2002)
27. Torrent M., Musaev D.G., Morokuma K., Ke S.-C., Warncke K.J.: J. Phys. Chem. B **103**, 8618–8627 (1999)
28. Torrent M., Mansour D., Day E.P., Morokuma K.: J. Phys. Chem. A **105**, 4546–4557 (2001)
29. Schiemann O., Fritscher J., Kisseleva N., Sigurdsson S.T., Prisner T.F.: ChemBioChem **4**, 1057–1065 (2003)
30. Fritscher J., Artin E., Wnuk S., Bar G., Robblee J.H., Kacprzak S., Kaupp M., Griffin R.G., Bennati M., Stubbe J.: J. Am. Chem. Soc. **127**, 7729–7738 (2005)
31. Schöneboom J.C., Neese F., Thiel W.: J. Am. Chem. Soc. **127**, 5840–5853 (2005)
32. Kacprzak S., Kaupp M., MacMillan F.: J. Am. Chem. Soc. **128**, 5659–5671 (2006)
33. Crofts A.R.,Wraight C.A.: Biochim. Biophys. Acta **726**, 149–185 (1983)
34. Nicholls D.G., Ferguson S.J.: Bioenergetics. London: Academic Press 2002.
35. Lubitz W., Feher G.: Appl. Magn. Reson. **17**, 1–48 (1999)
36. Stowell M.H.B., McPhillips T.M., Rees D.C., Soltis S.M., Abresch E., Feher G.: Science **276**, 812–816 (1997)
37. Flores M., Isaacson R., Abresch E., Calvo R., Lubitz W., Feher G.: Biophys. J. **90**, 3356–3362 (2006)
38. Breton J., Boullais C., Burie J.-R., Nabedryk E., Mioskowski C.: Biochemistry **33**, 14378–14386 (1994)
39. Brudler R., de Groot H.J.M., van Liemt W.B.S., Steggerda W.F., Esmeijer R., Gast P., Ho A.J., Lugtenburg J., Gerwert K.: EMBO J. **13**, 5523–5530 (1994)
40. Breton J., Nabedryk E.: Biochim. Biophys. Acta **1275**, 84–90 (1996)
41. Ermler U., Fritzsch G., Buchanan S.K., Michel H.: Structure **2**, 925–936 (1994)
42. Fritzsch G., Koepke J., Diem R., Kuglstatter A., Baciou L.: Acta Crystallogr. D **58**, 1660–1663 (2002)
43. Bittl R., Zech S.G.: J. Phys. Chem. B **101**, 1429–1436 (1997)
44. Prisner T.F., van der Est A., Bittl R., Lubitz W., Stehlik D., Möbius K.: Chem. Phys. **194**, 361–370 (1995)
45. Himo F., Babcock G.T., Eriksson L.A.: J. Phys. Chem. A **103**, 3745–3749 (1999)
46. Hutter M.C., Hughes J.M., Reimers J.R., Hush N.S.: J. Phys. Chem. B **103**, 4906–4915 (1999)
47. O'Malley P.: Chem. Phys. Lett. **285**, 99–104 (1998)
48. Nonella M.: J. Phys. Chem. B **102**, 4217–4225 (1998)
49. Boesch S.E., Wheeler R.A.: J. Phys. Chem. A **101**, 5799–5804 (1997)
50. Burie J.-R., Boullais C., Nonella M., Mioskowski C., Nabedryk E., Breton J.: J. Phys. Chem. B **101**, 6607–6617 (1997)
51. Nonella M., Mathias G., Eichinger M., Tavan P.: J. Phys. Chem. B **107**, 316–322 (2003)
52. O'Malley P.J.: Chem. Phys. Lett. **379**, 277–281 (2003)
53. Kacprzak S., Kaupp M.: J. Phys. Chem. B **108**, 2464–2469 (2004)
54. Harriman J.E.: Theoretical Foundations of Electron Spin Resonance. New York: Academic Press 1978.
55. Weltner W.: Magnetic Atoms and Molecules. New York: Dover Publications 1983.

56. Lucken E.A.C.: Nuclear Quadrupole Coupling Constants. New York: Academic Press 1969.
57. Gordy W.: Theory and Applications of Electron Spin Resonance. New York: Wiley 1980.
58. Tokman M., Sundholm D., Pyykkö P., Olsen J.: Chem. Phys. Lett. **265**, 60–64 (1997)
59. Bishop D. M., Cheung L.M.: Phys. Rev. A **20**, 381–384 (1979)
60. Pyykkö P.: Mol. Phys. **99**, 1617–1629 (2001)
61. Frisch M.J., Trucks G.W., Schlegel H.B., Scuseria G.E., Robb M.A., Cheeseman J.R., Zakrzewski V.G., Montgomery J.A. Jr., Stratmann R.E., Burant J.C., Dapprich S., Millam J.M., Daniels A.D., Kudin K.N., Strain M.C., Farkas O., Tomasi J., Barone V., Cossi M., Cammi R., Mennucci B., Pomelli C., Adamo C., Clifford S., Ochterski J., Petersson G.A., Ayala P.Y., Cui Q., Morokuma K., Salvador P., Dannenberg J.J., Malick D.K., Rabuck A.D., Raghavachari K., Foresman J.B., Cioslowski J., Ortiz J.V., Baboul A.G., Stefanov B.B., Liu G., Liashenko A., Piskorz P., Komaromi I., Gomperts R., Martin R.L., Fox D.J., Keith T., Al-Laham M.A., Peng C.Y., Nanayakkara A., Challacombe M., Gill P.M.W., Johnson B.G., Chen W., Wong M.W., Andres J.L., Gonzalez C., Head-Gordon M., Replogle E.S., Pople J.A.: Gaussian 98 (Revision A.11). Pittsburgh, Pa.: Gaussian, Inc. 2001.
62. Becke A.D.: J. Chem. Phys. **98**, 5648–5652 (1993)
63. Perdew J.P.: Physica B **172**, 1–6 (1991)
64. Perdew J.P., Wang Y.: Phys. Rev. B **45**, 13244–13249 (1992)
65. Stewart J.J.P.: J. Comput. Chem. **10**, 209–220 (1989)
66. Stewart J.J.P.: J. Comput. Chem. **10**, 221–264 (1989)
67. O'Malley P.: J. Phys. Chem. A **102**, 248–253 (1998)
68. O'Malley P.: J. Am. Chem. Soc. **120**, 5093–5097 (1998)
69. Kaupp M.: Biochemistry **41**, 2895–2900 (2002)
70. Salikhov K.M., Bock C.H., Stehlik D.: Appl. Magn. Reson. **1**, 195–211 (1990)
71. Lendzian F., Rautter J., Käß H., Gardiner A., Lubitz W.: Ber. Bunsenges. Phys. Chem. **100**, 2036–2040 (1996)
72. Spoyalov A.P., Hulsebosch R.J., Shochat S., Gast P., Hoff A.J.: Chem. Phys. Lett. **263**, 715–720 (1996)
73. Flores M., Isaacson R., Abresch E., Calvo R., Lubitz W., Feher G.: Biophys. J. **90**, 3356–3362 (2006)
74. Rohrer M., MacMillan F., Prisner T.F., Gardiner A., Möbius K., Lubitz W.: J. Phys. Chem. B **102**, 4648–4657 (1998)
75. Fritscher J.: Phys. Chem. Chem. Phys. **6**, 4950–4956 (2004)
76. Isaacson R.A., Abresch E.C., Lendzian F., Boullais C., Paddock M.L., Mioskowski C., Lubitz W., Feher G., in: The Reaction Center of Photosynthetic Bacteria: Structure and Dynamics (Michel-Beyerle M.-E., ed.). Berlin: Springer 1996.
77. Eriksson L.A., Himo F., Siegbahn P.E.M., Babcock G.T.: J. Phys. Chem. A **101**, 9496–9504 (1997)
78. Mattar S.M., Emwas A.H., Stephens A.D.: Chem. Phys. Lett. **363**, 152–160 (2002)

Authors' address: Jörg Fritscher, Institut für Physikalische und Theoretische Chemie and Center for Biomolecular Magnetic Resonance, J. W. Goethe-Universität, Max-von-Laue-Straße 7, 60438 Frankfurt am Main, Germany
E-mail: j.fritscher@epr.uni-frankfurt.de